Geophysical Research Letters

RESEARCH LETTER
10.1029/2019GL085665

Key Points:
- We turn deep earthquakes into virtual receivers by inter-source interferometry, to detect metastable olivine wedge in subducted slab
- We confirm the existence of the wedge about 30 km thick at 410-km depth and gradually thinning with depth to at least 580 km
- Our results suggest the slab core in transition zone is dry and deep-focus earthquakes initiate by the phase change of olivine

Supporting Information:
- Supporting Information S1

Correspondence to:
Z. Shen,
zshen@caltech.edu

Citation:
Shen, Z., & Zhan, Z. (2020). Metastable olivine wedge beneath the Japan Sea imaged by seismic interferometry. *Geophysical Research Letters*, *47*, e2019GL085665. https://doi.org/10.1029/2019GL085665

Received 6 OCT 2019
Accepted 26 FEB 2020
Accepted article online 29 FEB 2020

Metastable Olivine Wedge Beneath the Japan Sea Imaged by Seismic Interferometry

Zhichao Shen[1] **and Zhongwen Zhan**[1]

[1]Seismological Laboratory, California Institute of Technology, Pasadena, CA, USA

Abstract The metastable olivine wedge (MOW) within subducted slabs has long been hypothesized to host deep-focus earthquakes (>300 km). Its presence would also rule out hydrous slabs being subducted into the mantle transition zone. However, the existence and dimensions of MOW remain debatable. Here, we apply inter-source interferometry, which converts deep earthquakes into virtual seismometers, to detect the seismic signature of MOW without influence from shallow heterogeneities. With data from the Hi-net, we confirm the existence of MOW beneath the Japan Sea and constrain its geometry to be ~30 km thick at 410-km depth and gradually thinning to a depth of 580 km at least. Our result supports transformational faulting of metastable olivine as the initiation mechanism of deep earthquakes, although large events (*M*7.0+) probably rupture beyond the wedge. Furthermore, the slab core must be dehydrated at shallower depth and only transports negligible amount of water into the transition zone.

Plain Language Summary Most earthquakes occur within the top tens of kilometers of the Earth, but some can be more than 300 km deep. These deep earthquakes are puzzling, because they are not supposed to happen given the high pressure and temperature there. Scientists hypothesize that they might be caused by sudden phase changes of the mineral olivine, which should have broken down at the depth but survived metastably by hiding in the cold core of subducted plates. However, detecting the "surviving" metastable olivine has been difficult because of its small size and remoteness. Here we apply a novel method that can turn some deep earthquakes into virtual sensors closer to our target. Seismic waveforms recorded by these virtual sensors not only provide clear evidence for the metastable olivine but also constrain it dimension much better than before: a wedge 30 km thick at 410-km depth and extending down to 580-km depth at least. This finding supports the phase change hypothesis for deep earthquakes and also means that the slab core must be extremely dry, because even a small amount of water can break the "surviving" olivine mineral.

1. Introduction

Global earthquakes mostly occur in the crust but can extent to ~700-km depth within subducting plates. Crustal earthquakes are thought to be driven by the brittle frictional failure (Scholz, 1998), while the nature of deep-focus earthquakes (depth >300 km) has been posed to geophysicists as a long-standing puzzle (Brace & Kohlstedt, 1980). Several mechanisms have been proposed for deep earthquakes, including the dehydration embrittlement (Meade & Jeanloz, 1991), thermal shear instability (Kanamori et al., 1998; Ogawa, 1987) and transformational faulting (Green & Burnley, 1989). Among them, transformational faulting, which triggers the slip instability through a sudden phase change from metastable olivine to spinel, can naturally explain the depth dependent seismicity distribution that resurges in the transition zone with an abruptly cessation below 660 km (Houston, 2015). Moreover, recent laboratory experiments have shown fracture nucleation and later intense acoustic emissions associated with the olivine-to-spinel phase transformation (Schubnel et al., 2013; Wang et al., 2017), thus making the transformational faulting hypothesis more appealing.

For transformational faulting to happen, it is hypothesized that the low-pressure polymorphs of olivine inside cold slabs could metastably extend into the mantle transition zone (MTZ), forming a tongue-shaped "metastable olivine wedge" (MOW). Furthermore, the positively buoyant MOW, if present, may slow down the subducting slab in the MTZ (Bina et al., 2001), or even resist the slab from penetrating into the lower mantle (Tetzlaff & Schmeling, 2000). The dimension of MOW is generally thought to correlate with the slab thermal parameter (Kirby et al., 1996), but the water content of subducted slab and the latent

heat due to the phase changes also play crucial roles (Frane et al., 2013; Kubo et al., 1998; Mosenfelder et al., 2001). Laboratory experiments demonstrated that incorporation of a small amount of H_2O leads to a remarkable boost in the olivine to ringwoodite transformation rate via hydrolytic weakening process (Frane et al., 2013). The latent heat feedback together with an additional intracrystalline transformation mechanism significantly reduces the maximum depth that MOW can reach as suggested from an updated thermo-kinetic model (Mosenfelder et al., 2001). Therefore, the existence and exact geometry of MOW would provide essential constraints on the thermal-petrological properties of subducting slabs.

However, seismic imaging of the low-velocity MOW structure has been particularly challenging. For instance, body wave travel time analysis ubiquitously suffers from the wavefront healing effect. A thermal slab without MOW could satisfactorily predict high-resolution seismic arrival times, but the inclusion of MOW merely offers a subtle improvement on the data fitting (Koper et al., 1998). It has also been illustrated that the metastable olivine can be unveiled from waveform distortions of some seismic phases that travel through it (Koper & Wiens, 2000; Vidale et al., 1991). Nonetheless, deterministically examining the seismogram involves onerous effort because lithospheric heterogeneities contribute great complexities on the seismogram and smear the illumination of deep slab. Given the difficulty in resolving MOW, its thicknesses reported from preceding studies differ by more than a factor of 2 in Japan subduction zone (Furumura et al., 2016; Iidaka & Suetsugu, 1992; Jiang & Zhao, 2011; Kawakatsu & Yoshioka, 2011) (Table S1 in the supporting information), leaving the metastable persistence of olivine and its detail geometry hitherto ambiguous.

2. Inter-source Interferometry

To untangle the potentially subtle seismic signature of metastable olivine from complex shallow Earth heterogeneities, we apply inter-source interferometry (Curtis et al., 2009; Tonegawa & Nishida, 2010) to deep earthquake pairs in the Japan subduction zone (Figure 1a). For conventional inter-receiver interferometry, cross correlations of diffusive earthquake coda or ambient noise field reconstruct Green's functions between receiver pairs (Campillo & Paul, 2003). Equivalently, due to reciprocity, by cross-correlating coda waves from an earthquake pair, the inter-source interferometry synthesizes the transient strain triggered by passing seismic waves from one source to the other. This is as if we convert one of the deep earthquakes to a virtual seismometer deployed below the complex shallow layers and record the other event. To avoid violating the impulsive-source condition in reciprocity, we select five deep-focus earthquakes of small magnitudes ($4.0 \leq Mw \leq 5.2$) with simple source process (<10% non-double-couple component). Among them, three earthquakes (S1, S2, and S3) are refined at ~360-km depth whereas the other two (D1 and D2) are at depths of ~580 km (Figures S1 and S2; see the supporting information for relocation details), corresponding to the shallow and deep ends of hypothesized MOW, respectively. Although receivers in the inter-source interferometry should have a complete azimuthal coverage, the stationary phase approximation greatly loosens the receiver geometry restriction (Snieder, 2004; see the supporting information for inter-source interferometry). For our targeted slab beneath the Japan Sea, Hi-net stations situate around the stationary phase region of the deep earthquake pairs (the region along the extension of earthquake pairs; Figure 1b), hereby providing an ideal source-receiver configuration to isolate the deep slab structures from other complexities.

We first validate the inter-source interferometry method for two synthetic scenarios with and without MOW. The velocity and density profiles of slab and MOW are constructed based on a thermal model tuned for the Japan subduction zone (see the supporting information for modeling details). Small-scale heterogeneities are implemented at shallow depths to produce realistic coda waves (Figure 1b; Furumura & Kennett, 2005). Given the velocity and density profiles, we simulated the elastic wavefield with a GPU-based 2-D finite difference code in Cartesian coordinates, which is eighth order in space and second order in time (Li et al., 2014). With a minimum shear velocity of 2.8 km/s, a grid spacing of 75 m, and time step of 0.001 s, our computed synthetic waveforms are accurate up to 6 Hz with sampling of at least six grids per wavelength. Here, we simplified the problem into a 2-D slab geometry since we mainly focus on the updip direction. Moreover, 2-D and 3-D numerical simulations of the high-frequency trapping/guiding waves have been shown no significant differences (Kennett & Furumura, 2008; Takemura et al., 2015). After computing synthetic seismograms on the surface from deep earthquakes D1 and S1, we filter and cut the vertical-component coda waves from 5 to 45 s after the *P* wave first arrivals for interferometry. The 40-s-long window is further cut into 10-s-

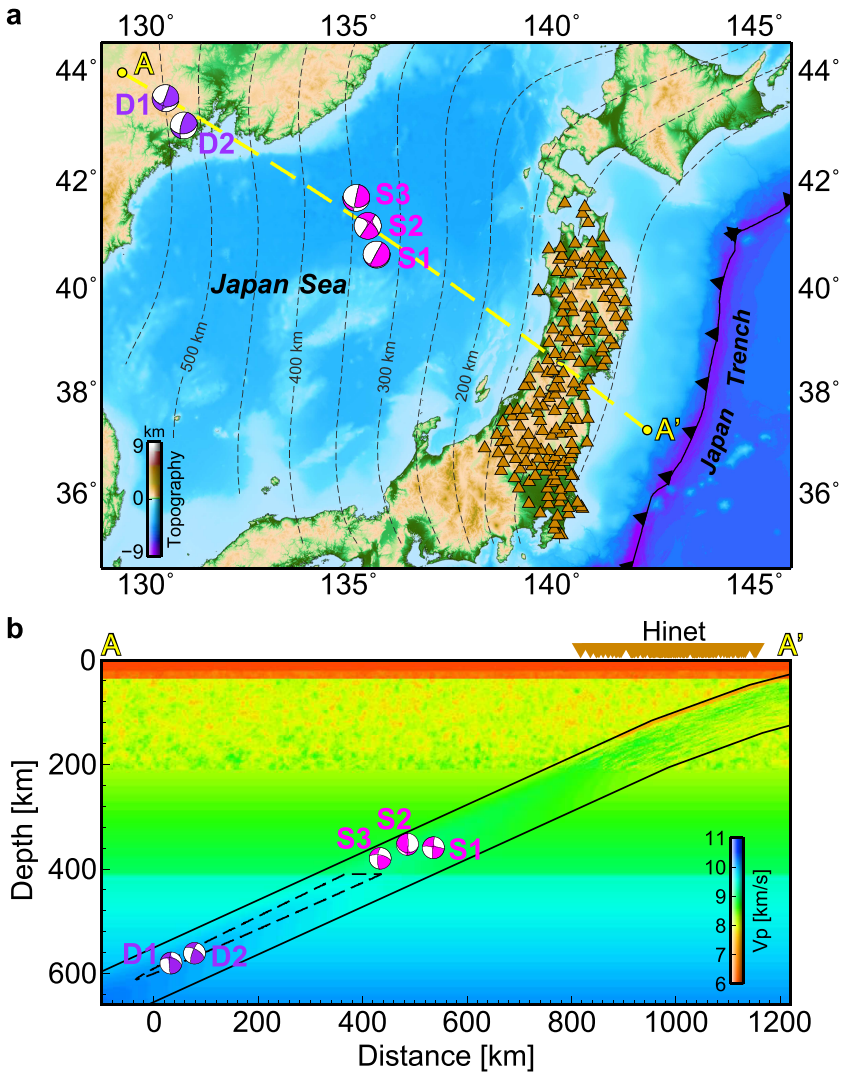

Figure 1. Map view of our targeted area and depth profile of Japan subduction zone. (a). Map of this study area. Black dashed lines are the slab depth contours from Slab2.0 model (Hayes et al., 2018). Orange triangles are Hi-net stations (Okada et al., 2004) used in our interferometry. The purple and magenta beach balls are from National Research Institute for Earth Science and Disaster Resilience (NIED) and represent the earthquake depths of ~580 km (D1 and D2) and ~360 km (S1, S2, and S3), respectively. (b). *P* wave velocity profile derived from thermal modeling along AA′. The black solid line and black dashed line represent the geometry of subducting Pacific slab and hypothesized MOW, respectively. Above 200-km depth, small-scale heterogeneities are included. D1/D2 and S1/S2/S3 correspond to the deep (~580 km) and shallow (~360 km) end of the MOW, respectively.

long overlapping segments offset by 2 s. The cross correlations of all the segments are then normalized by the maximum and averaged to account for the coda energy decay with time. For the D1-S1 earthquake pair in both scenarios, the 0.2-2 Hz cross-correlation record section presents coherent waveforms with constant arrival time across the profile of Hi-net (Figure S3). This indicates that our simulated coda wavefields are diffuse due to shallow heterogeneities and the inter-source Green's function could be extracted by coda interferometry at a single station (Snieder, 2004). To enhance the coherent signal, we stack the cross correlations over all the stations. In both scenarios with and without MOW, the resulting interferometric waveforms match the directly simulated *P* wave strain seismograms from source D1 to virtual receiver S1 and, meanwhile, capture the polarity flip (Figure S3b vs. Figure S3c) caused by the reverberation of *P* wave within the MOW (Figure S4). For the case with MOW, although the *P* refraction wave arrives earlier than the reverberation, its energy is too weak to be captured (Figure S4f). Since absolute arrival times have strong trade-offs with earthquake locations, herein, we focus solely on interpreting the waveform shape.

3. Results

Having shown the feasibility to retrieve the *P* wave strain Green's functions between two deep earthquakes, we apply the inter-source interferometry method to real data on the Hi-net stations (Figure 1). As an example, the cross-correlation record section for the D1-S1 earthquake pair at 0.2–2 Hz exhibits coherent signals arriving at a constant time in a wide azimuth range (Figure 2a), implying a diffuse coda wavefield. After stacking all the individual cross correlations, the resulting waveform presents a negative trough preceding a positive peak, similar to that of aforementioned synthetic case with a MOW (Figure 2c). Furthermore, the interferometric results of other earthquake pairs are in good agreement with that of D1-S1 pair (Figure S5), favoring a MOW structure instead of a simple slab model without MOW (Figures S6a and S6b). Note that there are some waveform differences among our observed waveforms (e.g., weakening of positive phase after the negative phase: D1-S2 vs. D2-S2). In fact, those differences can be explained by the location difference between D1 and D2, which will be shown later. Beside the MOW cause, we also scrutinize other alternatives that could result in the negative pulse, such as opposite focal mechanisms and a low-velocity hydrous oceanic crust on top of the slab. First motion analysis shows that the Hi-net stations used for interferometry share same *P* wave polarities for all the selected deep earthquakes (Figures 2b and S7), so radiation patterns alone cannot explain the negative polarities of the correlations. An 8-km-thick oceanic crust with a velocity reduction of 8% extending to 660 km fails to reproduce our observations as well (Figures 2c and S8). With these alternative possibilities ruled out, we suggest the existence of metastable olivine beneath the Japan Sea as the preferred interpretation.

To better quantify the MOW dimension and depth extent, which are both important for understanding deep earthquake physics and slab hydrous state, we need to appeal to higher frequency interferometric waveforms. For example, we show that the 0.2-2 Hz cross-correlation waveforms are insensitive to the location of S1/S2/S3 relative to the MOW (Figure S9), which in turn provide little information on the thickness of MOW at the shallow end. On the other hand, at 0.2–5 Hz, synthetic strains are significantly distorted across a short distance range (Figure S9). The rapid high-frequency waveform variations are due to the receiver locations with respect to the *P* multiples (Figures S4e, S4f, and S9d–S9f). Hence, with well-constrained relative locations among the virtual sensors S1, S2, and S3, we can use higher frequency (up to 5 Hz) waveform details at different locations to determine the geometry of metastable olivine. Indeed, for synthetic tests with a set of earthquake pairs, the inter-source interferometry is shown to be capable of extracting 5-Hz transient strains and capturing the waveform variations at different virtual sensors (Figure S10). Furthermore, 15° variation in focal mechanisms (Kubo et al., 2002) barely changes the stacked strain waveform shapes in our synthetic tests (Figure S10d).

Subsequently with the real data from Hi-net, we retrieve the 0.2-5 Hz strain responses for all six earthquake pairs from D1/D2 to S1/S2/S3 following the same interferometry procedures (Figure S11). Taking D1 as an example, virtual sensor S1 records a simple trace with negative polarity, but the other two (S2 and S3) present splitting waveforms that consist of two phases (Figure 3c). To evaluate the robustness of observed waveform complexity, we estimated their noise level by computing the 95% confidence intervals for stacked cross correlations using a bootstrapping technique (Figure S12). All the coherent signals among D1-S1/S2/S3 evidently stand above the noise level; thus, the traces characterized by splitting phases are unlikely caused by noise (Figure S12). Also, S1 and S3 have similar beachballs but present apparent waveform variations, ruling out the focal mechanism cause. Instead, the distinct interferometric waveforms appear to correlate with the spatial distribution of virtual sensors: S2 and S3 with splitting phases are close to the slab upper interface, whereas S1 with a single phase sits near the slab core (Figure 3a). In addition, similar interferometric results from the other deep earthquake D2, though with higher noise levels (Figure 3c).

To account for these high-frequency waveform variations, we grid-searched a variety of MOW geometries through physics-based modeling. Assuming that temperature is the first-order control on the olivine phase transformation, the MOW would thus be defined as the region colder than a kinetic cutoff temperature (T_{mow}) in our initial thermal slab. In searching for the optimal MOW geometry to fit our interferometric observations, we directly computed the synthetic waveforms at virtual seismometer S1/S2/S3 from deep earthquake D1/D2. When comparing the synthetics with observations, we tested different kinetic kick-off temperatures as well as the deep earthquake locations relative to MOW allowing a maximum arrival time difference of 1.5 s. We found that both 0.2-2 and 0.2-5 Hz interferometric waveforms can be adequately

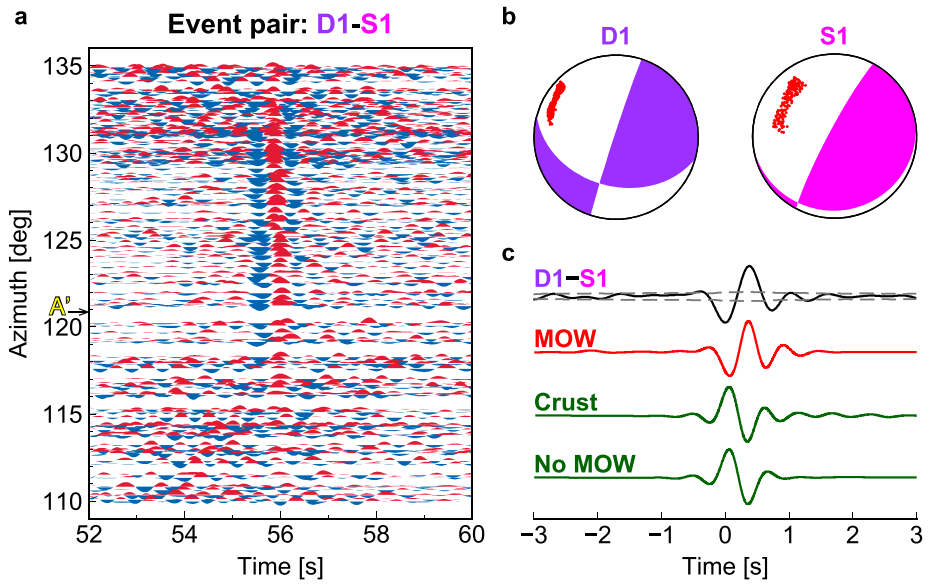

Figure 2. Inte-rsource interferometry results at 0.2–2 Hz suggest the existence of metastable olivine beneath the Japan Sea. (a). The record section of coda wave cross correlations as a function of azimuth for the D1-S1 earthquake pair. The azimuth (120.7°) of AA′ profile in Figure 1 is shown as A′ with a black arrow. Blue and red color correspond to the negative and positive phases, respectively. Coherent signals with negative polarities arrive at a constant time across Hi-net stations. (b). First motion analysis for deep earthquakes D1 and S1. At Hi-net stations (red dots), both events share the same *P* wave polarities. (c). Waveform comparison of observations and synthetics. The top black trace is the stacked cross-correlation waveform from all the traces shown in (a) for D1-S1 deep earthquake pair. The gray dashed lines denote the noise level. The red and dark green lines are the synthetic strain waveforms for cases of a thermal slab with MOW (MOW), a thermal slab with hydrous oceanic crust (Crust), and a thermal slab only (No MOW), respectively. All the traces are aligned by their peak phases. Only the MOW model predicts the waveform shape observed in D1-S1 pair.

fitted when T_{mow} is defined as 664 °C with D1 and D2 situating close to, but at different distances from, the lower boundary of metastable olivine (Figure 3). The resolved *P* wave velocity within MOW is 4–5% lower than the surrounding slab velocity (2–3% lower than that of ambient mantle; Figure S13), which is consistent with previous studies (Furumura et al., 2016; Jiang & Zhao, 2011). Furthermore, our MOW

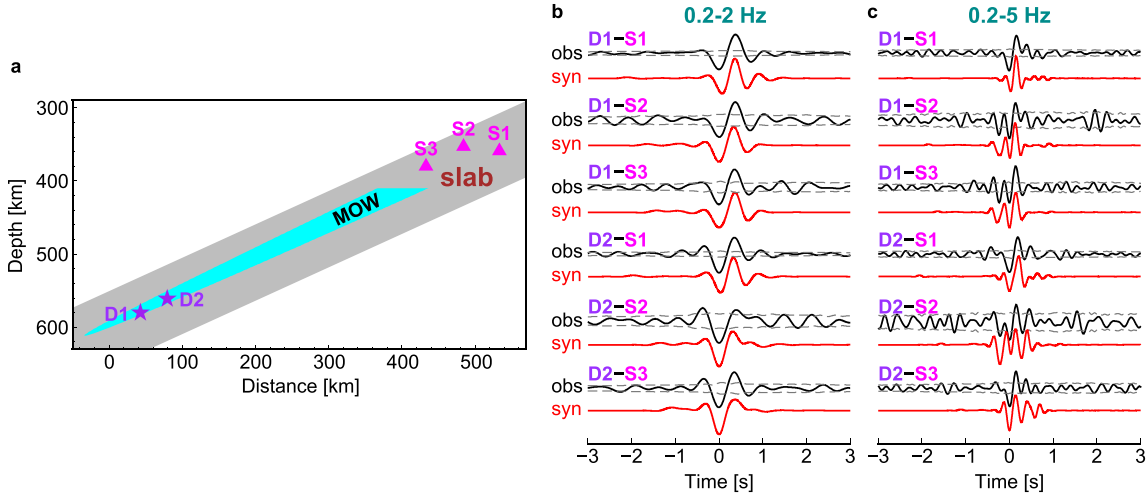

Figure 3. Proposed MOW dimension can reproduce our inter-source interferometry observations. (a). Slab profile with deep earthquakes D1/D2 and three virtual receivers (S1–S3). The gray and cyan region denote the slab and our proposed MOW, respectively. The *P* wave velocity within MOW decreases 5%. Both D1 and D2 need to be within MOW to explain the interferometric waveforms. (b). The 0.2-2 Hz waveform comparison of inter-source interferometric observations (black lines) and synthetics (red lines) for all deep earthquake pairs. The gray dashed lines denote the noise level. (c) Similar to (b) but for higher frequency up to ~5 Hz. All six waveforms are well fitted by our suggested MOW model.

model also provides a good fit to interferometric observations at the three virtual receivers from the other deep earthquake D2 (Figure 3). For instance, as discussed earlier, the observed D2-S2/S3 2-Hz waveform presents a much weaker positive phase after the negative one than that of D1-S2/S3 (Figure 3b). These waveform differences are well captured by our MOW model, while a simple slab model cannot produce such waveform variations (Figures S6a–S6c). Despite that the 2-Hz and 5-Hz interferometric waveform details are not fully explained due to lateral variations in slab structures, the observed waveform features (polarities, single, or splitting phases) are generally retained in synthetic seismograms. Given the same thermal model, neither a thinner MOW (T_{mow} = 620 °C) and a thicker MOW (T_{mow} = 720°C) can reproduce most of the 5-Hz observations (Figures S6d–S6i). Moreover, we computed the waveform similarity among observations and synthetics for a variety of T_{mow} models. The allowed MOW dimension is quantified to a narrow range of T_{mow} (Figure S14), corresponding to 28–30 km thick at 410 km and gradually thinning to a depth of 600–620 km. Here, we emphasize that our new interferometry observations constrain the MOW geometry and velocity reduction, instead of the cutoff temperature (T_{mow}) or the thermal model. For scenarios with different combinations of slab parameters (e.g., subduction rate and age), T_{mow} that fits the data best can vary by tens of degrees (Figure S15). Nonetheless, the MOW structures consistently resemble a thickness of ~30 km across the slab at 410 km and gradually diminish to a depth of ~610 km at least. We also test a few different MOW models by varying its thicknesses at ~610 km (Figure S16a) to reduce the thermal constrain to some extent. MOWs thicker than ~20 km at bottom cannot reproduce our observed waveforms (Figures S16b–S16d), suggesting that the thinning of MOW is required. Still, it is possible that MOW can extend to greater depth (Figure 4), since our inter-source interferometry method cannot resolve even deeper slab structure due to our current deep earthquake geometry (Figure S16b).

4. Discussion and Conclusions

Compared to previously proposed MOW geometries in nearby regions, our MOW at 410-km depth is similar to that imaged by the receiver function (Kawakatsu & Yoshioka, 2011) but considerably thinner than that derived from travel time-based studies (Table S1). With our resolved MOW dimension, the delay of olivine phase transformation is estimated to increase the slab buoyancy by 1% below 410 km, which is comparable to the thermal slab buoyancy force (2–3%; Cammarano et al., 2003). Such extra buoyancy force generated by the metastable olivine could in turn reduce the slab subduction rate (Tetzlaff & Schmeling, 2000). Given the age of Japan trench (Sdrolias & Müller, 2006), the associated metastable olivine for a 130-Ma oceanic lithosphere is estimated to slow down the subduction rate by up to ~12% (Bina et al., 2001). For colder slabs, such as Tonga, the effect might be even stronger, due to the presumably larger MOW. In our preferred scenario (Figure 4), deep earthquakes D1 and D2 occur within MOW, supporting transformational faulting as the cause of deep earthquakes. Assuming a circular crack and a constant strain drop (Vallée, 2013), the metastable olivine thickness at 600-km depth is equivalent to the dimension of a moderate-magnitude earthquake (*Mw*7) that ruptures across the slab. To host larger deep earthquakes (e.g., *Mw*7+) with larger rupture dimensions, which did occur beneath the Japan Sea and in other warmer subduction zones with potentially thinner MOWs, the slip instability probably nucleates within MOW by transformational faulting and later propagate outside driven by other mechanisms (e.g., the thermal shear instability). The switch of mechanism around *M*6–7 would break the self-similarity of deep earthquake sizes and cause a change in the Gutenberg-Richter distributions (i.e., *b* values), which is recently observed (Zhan, 2017). Furthermore, models of great deep earthquakes, such as the 1994 *Mw*8.2 Bolivia earthquake and the 2018 *Mw*8.0 Fiji-Tonga doublet, also imply two-stage rupture processes and exemplify local slab temperature as the critical factor for deep earthquakes (Jia et al., 2020; Zhan et al., 2014).

The depth extent of our proposed MOW indicates an extremely dry Pacific slab core (<75 wt ppm) in the MTZ beneath the Japan Sea (Figure 4; Kawakatsu & Yoshioka, 2011; Frane et al., 2013). However, the arc volcanism, intermediate-depth earthquakes, and high-resolution tomography models all point to substantially hydrated slab above 200-km depth (Cai et al., 2018; Hasegawa & Nakajima, 2017), potentially through outer-rise plate-bending faults that cut deep into the incoming plate as pathways for water (Ranero et al., 2003). Therefore, the water associated with these faults must be expelled almost completely into the mantle at intermediate depths (Kawakatsu & Watada, 2007), carrying negligible amount of water into the MTZ (Green et al., 2010). Conversely, garnering evidences from ultradeep diamond inclusions (Pearson et al., 2014), mineral experiments (Kohlstedt et al., 1996) and electromagnetic induction data (Kelbert et al.,

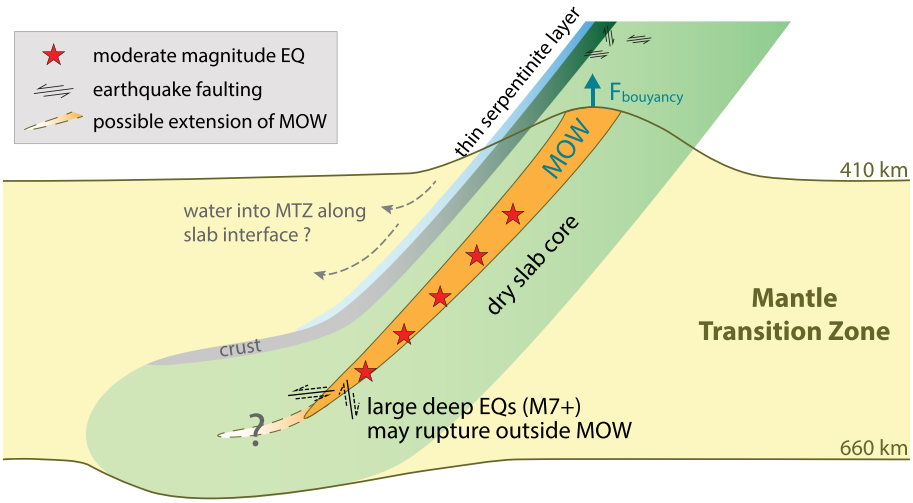

Figure 4. Schematic cross section of subducted slab in the mantle transition zone. Metastable olivine persists in the slab core as a wedge extending down to the bottom of MTZ. The red stars indicate moderate-magnitude earthquakes. Deep earthquakes can initiate within MOW by transformational faulting, but larger deep earthquakes (black dashed faulting) may potentially rupture outside MOW driven by other mechanisms. The existence of MOW requires that the core of subducted slab must carries negligible amount of water. But it is still possible that the water can be transported into the mantle transition zone along the slab interface.

2009) have demonstrated that the MTZ can, at least locally, harbor substantial amount of water (up to ~2.5 wt%). Given the distance between our MOW and plate interface (~24 km) and the hydrogen diffusion coefficients of olivine and its polymorphs (Hae et al., 2006), it is still possible that a thin layer near the subducting plate provide potential pathways for transporting water into MTZ, such as a narrow serpentinite channel on top of the slab (Kawakatsu & Watada, 2007). Or instead of linking the water reservoir in MTZ to current subduction, the wet MTZ might be possibly associated with other tectonic processes (Green et al., 2010; Hirschmann, 2006).

Acknowledgments
We are grateful to Micheal Gurnis, Paul Asimow, Sidao Ni, and Wenbo Wu for discussions and suggestions. We are also grateful for reviews from two anonymous reviewers, which helped to improve the manuscript. Seismic data are collected from the Data Management Center of the Incorporated Research Institutions for Seismology (https://www.iris.edu/dms/nodes/dmc), Hi-net (http://www.hinet.bosai.go.jp/) and F-net (http://www.fnet.bosai.go.jp/). The earthquake catalog and focal mechanisms are downloaded from ISC-EHB distributed by the International Seismological Centre (ISC, http://www.isc.ac.uk/) and National Research Institute for Earth Science and Disaster Resilience (NIED, http://www.fnet.bosai.go.jp/event/search.php?LANG=en). The earthquake arrival time data is available at the Japan Meteorological Agency (JMA, http://www.data.jma.go.jp/svd/eqev/data/bulletin/index_e.html).

References

Bina, C. R., Stein, S., Marton, F. C., & Van Ark, E. M. (2001). Implications of slab mineralogy for subduction dynamics. *Physics of the Earth and Planetary Interiors*, *127*(1-4), 51–66.

Brace, W. F., & Kohlstedt, D. L. (1980). Limits on lithospheric stress imposed by laboratory experiments. *Journal of Geophysical Research*, *85*(B11), 6248–6252.

Cai, C., Wiens, D. A., Shen, W., & Eimer, M. (2018). Water input into the Mariana subduction zone estimated from ocean-bottom seismic data. *Nature*, *563*(7731), 389–392. https://doi.org/10.1038/s41586-018-0655-4

Cammarano, F., Goes, S., Vacher, P., & Giardini, D. (2003). Inferring upper-mantle temperatures from seismic velocities. *Physics of the Earth and Planetary Interiors*, *138*(3-4), 197–222.

Campillo, M., & Paul, A. (2003). Long-range correlations in the diffuse seismic coda. *Science*, *299*(5606), 547–549. https://doi.org/10.1126/science.1078551

Curtis, A., Nicolson, H., Halliday, D., Trampert, J., & Baptie, B. (2009). Virtual seismometers in the subsurface of the Earth from seismic interferometry. *Nature Geoscience*, *2*(10), 700.

Frane, D. W. L., Sharp, T. G., Mosenfelder, J. L., & Leinenweber, K. (2013). Ringwoodite growth rates from olivine with ~75 ppmw H_2O: metastable olivine must be nearly anhydrous to exist in the mantle transition zone. *Physics of the Earth and Planetary Interiors*, *219*, 1–10.

Furumura, T., Kennett, B. L., & Padhy, S. (2016). Enhanced waveguide effect for deep-focus earthquakes in the subducting Pacific slab produced by a metastable olivine wedge. *Journal of Geophysical Research: Solid Earth*, *121*, 6779–6796. https://doi.org/10.1002/2016JB013300

Furumura, T., & Kennett, B. L. N. (2005). Subduction zone guided waves and the heterogeneity structure of the subducted plate: Intensity anomalies in northern Japan. *Journal of Geophysical Research*, *110*, B10302. https://doi.org/10.1029/2004JB003486

Green, H. W. II, & Burnley, P. C. (1989). A new self-organizing mechanism for deep-focus earthquakes. *Nature*, *341*(6244), 733.

Green, H. W. II, Chen, W. P., & Brudzinski, M. R. (2010). Seismic evidence of negligible water carried below 400-km depth in subducting lithosphere. *Nature*, *467*(7317), 828–831. https://doi.org/10.1038/nature09401

Hae, R., Ohtani, E., Kubo, T., Koyama, T., & Utada, H. (2006). Hydrogen diffusivity in wadsleyite and water distribution in the mantle transition zone. *Earth and Planetary Science Letters*, *243*(1-2), 141–148.

Hasegawa, A., & Nakajima, J. (2017). Seismic imaging of slab metamorphism and genesis of intermediate-depth intraslab earthquakes. *Progress in Earth and Planetary Science*, *4*(1), 12.

Hayes, G. P., Moore, G. L., Portner, D. E., Hearne, M., Flamme, H., Furtney, M., & Smoczyk, G. M. (2018). Slab2, a comprehensive subduction zone geometry model. *Science*, *362*(6410), 58–61. https://doi.org/10.1126/science.aat4723

Hirschmann, M. M. (2006). Water, melting, and the deep Earth H_2O cycle. *Annual Review of Earth and Planetary Sciences*, *34*, 629–653.

Houston, H. (2015). 4.13—Deep earthquakes. In G. Schubert (Ed.), *Treatise on geophysics* (2nd ed., pp. 329–354). Oxford: Elsevier. https://doi.org/10.1016/B978-0-444-53802-4.00079-8

Iidaka, T., & Suetsugu, D. (1992). Seismological evidence for metastable olivine inside a subducting slab. *Nature*, *356*(6370), 593–595.

Jia, Z., Shen, Z., Zhan, Z., Li, C., Peng, Z., & Gurnis, M. (2020). The 2018 Fiji *Mw* 8.2 and 7.9 deep earthquakes: One doublet in two slabs. *Earth and Planetary Science Letters*, *531*. https://doi.org/10.1016/j.epsl.2019.115997

Jiang, G., & Zhao, D. (2011). Metastable olivine wedge in the subducting Pacific slab and its relation to deep earthquakes. *Journal of Asian Earth Sciences*, *42*(6), 1411–1423.

Kanamori, H., Anderson, D. L., & Heaton, T. H. (1998). Frictional melting during the rupture of the 1994 Bolivian earthquake. *Science*, *279*(5352), 839–842. https://doi.org/10.1126/science.279.5352.839

Kawakatsu, H., & Watada, S. (2007). Seismic evidence for deep-water transportation in the mantle. *Science*, *316*(5830), 1468–1471. https://doi.org/10.1126/science.1140855

Kawakatsu, H., & Yoshioka, S. (2011). Metastable olivine wedge and deep dry cold slab beneath southwest Japan. *Earth and Planetary Science Letters*, *303*(1-2), 1–10.

Kelbert, A., Schultz, A., & Egbert, G. (2009). Global electromagnetic induction constraints on transition-zone water content variations. *Nature*, *460*(7258), 1003–1006. https://doi.org/10.1038/nature08257

Kennett, B. L. N., & Furumura, T. (2008). Stochastic waveguide in the lithosphere: Indonesian subduction zone to Australian craton. *Geophysical Journal International*, *172*(1), 363–382.

Kirby, S. H., Stein, S., Okal, E. A., & Rubie, D. C. (1996). Metastable mantle phase transformations and deep earthquakes in subducting oceanic lithosphere. *Reviews of Geophysics*, *34*(2), 261–306.

Kohlstedt, D. L., Keppler, H., & Rubie, D. C. (1996). Solubility of water in the α, β and γ phases of $(Mg, Fe)_2SiO_4$. *Contributions to Mineralogy and Petrology*, *123*(4), 345–357.

Koper, K. D., & Wiens, D. A. (2000). The waveguide effect of metastable olivine in slabs. *Geophysical Research Letters*, *27*(4), 581–584.

Koper, K. D., Wiens, D. A., Dorman, L. M., Hildebrand, J. A., & Webb, S. C. (1998). Modeling the Tonga slab: Can travel time data resolve a metastable olivine wedge? *Journal of Geophysical Research*, *103*(B12), 30,079–30,100.

Kubo, A., Fukuyama, E., Kawai, H., & Nonomura, K. I. (2002). NIED seismic moment tensor catalogue for regional earthquakes around Japan: Quality test and application. *Tectonophysics*, *356*(1-3), 23–48.

Kubo, T., Ohtani, E., Kato, T., Shinmei, T., & Fujino, K. (1998). Effects of water on the α-β transformation kinetics in San Carlos olivine. *Science*, *281*(5373), 85–87. https://doi.org/10.1126/science.281.5373.85

Li, D., Helmberger, D., Clayton, R. W., & Sun, D. (2014). Global synthetic seismograms using a 2-D finite-difference method. *Geophysical Journal International*, *197*(2), 1166–1183.

Meade, C., & Jeanloz, R. (1991). Deep-focus earthquakes and recycling of water into the Earth's mantle. *Science*, *252*(5002), 68–72. https://doi.org/10.1126/science.252.5002.68

Mosenfelder, J. L., Marton, F. C., Ross, C. R. II, Kerschhofer, L., & Rubie, D. C. (2001). Experimental constraints on the depth of olivine metastability in subducting lithosphere. *Physics of the Earth and Planetary Interiors*, *127*(1-4), 165–180.

Ogawa, M. (1987). Shear instability in a viscoelastic material as the cause of deep focus earthquakes. *Journal of Geophysical Research*, *92*(B13), 13,801–13,810.

Okada, Y., Kasahara, K., Hori, S., Obara, K., Sekiguchi, S., Fujiwara, H., & Yamamoto, A. (2004). Recent progress of seismic observation networks in Japan—Hi-net, F-net, K-NET and KiK-net. *Earth, Planets and Space*, *56*(8).

Pearson, D. G., Brenker, F. E., Nestola, F., McNeill, J., Nasdala, L., Hutchison, M. T., et al. (2014). Hydrous mantle transition zone indicated by ringwoodite included within diamond. *Nature*, *507*(7491), 221–224. https://doi.org/10.1038/nature13080

Ranero, C. R., Morgan, J. P., McIntosh, K., & Reichert, C. (2003). Bending-related faulting and mantle serpentinization at the Middle America trench. *Nature*, *425*(6956), 367–373. https://doi.org/10.1038/nature01961

Scholz, C. H. (1998). Earthquakes and friction laws. *Nature*, *391*(6662), 37–42.

Schubnel, A., Brunet, F., Hilairet, N., Gasc, J., Wang, Y., & Green, H. W. (2013). Deep-focus earthquake analogs recorded at high pressure and temperature in the laboratory. *Science*, *341*(6152), 1377–1380. https://doi.org/10.1126/science.1240206

Sdrolias, M., & Müller, R. D. (2006). Controls on back-arc basin formation. *Geochemistry, Geophysics, Geosystems*, *7*, Q04016. https://doi.org/10.1029/2005GC001090

Snieder, R. (2004). Extracting the Green's function from the correlation of coda waves: A derivation based on stationary phase. *Physical Review E*, *69*(4), 046610.

Takemura, S., Yoshimoto, K., & Tonegawa, T. (2015). Velocity increase in the uppermost oceanic crust of subducting Philippine Sea plate beneath the Kanto region due to dehydration inferred from high-frequency trapped P waves. *Earth, Planets and Space*, *67*(1), 41.

Tetzlaff, M., & Schmeling, H. (2000). The influence of olivine metastability on deep subduction of oceanic lithosphere. *Physics of the Earth and Planetary Interiors*, *120*(1-2), 29–38.

Tonegawa, T., & Nishida, K. (2010). Inter-source body wave propagations derived from seismic interferometry. *Geophysical Journal International*, *183*(2), 861–868.

Vallée, M. (2013). Source time function properties indicate a strain drop independent of earthquake depth and magnitude. *Nature Communications*, *4*, 2606. https://doi.org/10.1038/ncomms3606

Vidale, J. E., Williams, Q., & Houston, H. (1991). Waveform effects of a metastable olivine tongue in subducting slabs. *Geophysical Research Letters*, *18*(12), 2201–2204.

Wang, Y., Zhu, L., Shi, F., Schubnel, A., Hilairet, N., Yu, T., et al. (2017). A laboratory nanoseismological study on deep-focus earthquake micromechanics. *Science Advances*, *3*(7), e1601896. https://doi.org/10.1126/sciadv.1601896

Zhan, Z. (2017). Gutenberg–Richter law for deep earthquakes revisited: A dual-mechanism hypothesis. *Earth and Planetary Science Letters*, *461*, 1–7.

Zhan, Z., Kanamori, H., Tsai, V. C., Helmberger, D. V., & Wei, S. (2014). Rupture complexity of the 1994 Bolivia and 2013 Sea of Okhotsk deep earthquakes. *Earth and Planetary Science Letters*, *385*, 89–96.